Journal of Photochemistry and Photobiology 11 (2022) 100136

Contents lists available at ScienceDirect

Journal of Photochemistry and Photobiology

journal homepage: www.sciencedirect.com/journal/journal-of-photochemistry-and-photobiology

Active targeted photodynamic therapeutic effect of silver-based nanohybrids on melanoma cancer cells

Hanieh Montaseri, Nkune Williams Nkune, Heidi Abrahamse *

Laser Research Centre, Faculty of Health Sciences, University of Johannesburg, P.O. Box 17011, Doornfontein 2028, South Africa

ARTICLE INFO

Keywords:
Silver-based nanohybrids
Zinc phthalocyanine tetrasulfonate
Targeted photodynamic therapy
Melanoma cancer

ABSTRACT

Malignant melanoma is aggressive cancer that metastasizes along with the heterogeneity at the molecular and cellular levels, thereby reducing overall therapeutic efficacy. In the present research, the concept of photodynamic therapy (PDT) was investigated on silver-based nanohybrids for the treatment of A375 melanoma cancer cells. Hence, two different nanoparticles (NPs) namely Ag-PEG NPs and core/shell Ag@mSiO$_2$ NPs were fabricated and conjugated to zinc phthalocyanine tetrasulfonate (ZnPcS$_4$) photosensitizer (PS). Folic acid (FA) as a targeting moiety was also decorated onto the surface of nanohybrids to selectively target the folate receptors that are overexpressed on the A375 cells. Ultimately, the PDT efficacy of both ZnPcS$_4$/Ag-PEG-FA and ZnPcS$_4$/Ag@mSiO$_2$-FA nanohybrids were compared via ATP viability, flow cytometry, and reactive oxygen species (ROS) assays. The obtained near-spherical shaped nanohybrids had zeta potential of -4.03 ± 0.3 mV for ZnPcS$_4$/Ag-PEG-FA, and -14.4 ± 0.6 mV for the ZnPcS$_4$/Ag@mSiO$_2$-FA. A significant PDT effect was observed for the cells exposed to 674 nm laser irradiation after incubation with ZnPcS$_4$/Ag@mSiO$_2$-FA with ~92%* ± 1.1 cell death compared to ~70%* ± 2.9 cell death for ZnPcS$_4$/Ag-PEG-FA nanohybrids owing to the higher generation of ROS for the former nanohybrids. The majority of the cell death was induced via apoptosis rather than necrosis as the nanohybrids successfully localized in mitochondria. The overall finding of this study concluded that an active targeting strategy significantly enhanced the cellular uptake of the nanohybrids compared to passive targeting. Moreover, strong surface plasmon-PS resonance coupling in ZnPcS$_4$/Ag@mSiO$_2$-FA nanohybrids enhanced singlet oxygen generation in comparison to the PS alone or ZnPcS$_4$/Ag-PEG-FA nanohybrids.

1. Introduction

Melanoma is the most aggressive type of skin cancer which is caused by genetic mutations in melanocytes [1]. Current therapeutic modalities include surgical resection, radiotherapy, chemotherapy, immunotherapy, and photodynamic therapy (PDT). Although chemotherapy with therapeutic agents such as dacarbazine and temozolomide is an important palliative treatment of progressive melanomas [2], resistance to apoptosis is the main cause of chemotherapy drug resistance in melanoma cancer [3]. In this regard, PDT is considered an adjuvant and minimally invasive procedure for patients with stage III/IV cutaneous metastatic melanomas [4]. PDT is a successful curative modality for premalignant and early disease and is deemed an effective palliative therapy for late-stage disease [5]. A photosensitizer (PS), which is absorbed in metabolically active tissues, and an appropriate wavelength of light to activate the PS are indispensable parts of PDT [1].

Zinc phthalocyanine derivatives are promising second-generation PSs in PDT. They provide unique advantages compared to other PSs by high affinity towards neovascular tissues with a high photosensitizing ability [6]. In addition, rapid tissue uptake with low cytotoxicity and skin photosensitization have made them reliable PSs in PDT [7]. More importantly, their long-wavelength absorption peak at around 670 nm can facilitate the penetration of exciting light for the treatment of deep-seated tumors [6]. Among phthalocyanine PSs, zinc phthalocyanine tetrasulfonate (ZnPcS$_4$) has been more investigated in PDT. It is a strongly hydrophilic PS due to the presence of sulfonate groups [8]. Additionally, it efficiently generates singlet oxygen with peak absorption in the ultraviolet and red ranges between 670 and 680 nm [6].

Despite significant advantages of the ZnPcS$_4$ PS in PDT, the large conjugated π-system leads to a strong stacking tendency in aqueous solution thereby decreasing its luminescence quantum yield and photosensitizing efficiency [8] as only monomeric species of the PSs are photoactive [9]. In this sense, drug delivery systems as vehicles have been introduced to change their photophysical properties,

* Corresponding author.
E-mail address: habrahamse@uj.ac.za (H. Abrahamse).

https://doi.org/10.1016/j.jpap.2022.100136
Received 5 April 2022; Received in revised form 5 July 2022; Accepted 12 July 2022
Available online 14 July 2022

biocompatibility and solubility nature, and PDT efficacy [10]. In addition, drug delivery systems enable the delivery of the PSs to the targeted site and direct injection into the bloodstream [11].

Nanoparticles (NPs) based on silver, gold, platinum, and iron metal have been extensively studied as drug and gene delivery, contrast and PDT agents, and fluorescence cell imaging [12,13]. There are several reports regarding the incorporation of metal NPs with phthalocyanine PSs. However, the literature review notes that limited silver-phthalocyanine-based hybrids have been developed as PDT agents which motivated us to design and synthesize such potential systems and check their PDT effects. Remarkably, the spectral overlap between the absorption band of the $ZnPcS_4$ PS and the localized surface plasmon resonance (LSPR) absorption band of silver-based NPs could enhance the production of singlet oxygen resulting in improving PDT efficacy [10].

In the present investigation, two different silver-based nanoparticles, Ag-PEG and core/shell $Ag@mSiO_2$ NPs were fabricated and incorporated with $ZnPcS_4$ PS. The resultant nanohybrids were then conjugated to folic acid (FA) to promote active targeting moieties to investigate their photodynamic therapeutic effects on A375 melanoma cancer cells. Ultimately the PDT effect of both nanohybrids was compared to explore the best choice for potential use in PDT of A375 cells.

2. Materials and methods

2.1. Materials

Silver nitrate ($AgNO_3$, ACS reagent, ≥99.0%), tri-sodium citrate (for molecular biology, ≥99%), tannic acid (ACS reagent), dimethyl sulfoxide (DMSO, anhydrous, ≥99.9%), SH-PEG_{2k}-NH_2 (HCl salt, average Mn 2000), N-ethyl-N′-(3-dimethyl aminopropyl) carbodiimide (EDC, BioXtra), N-hydroxysuccinimide (NHS, 98%), folic acid (FA, ≥97%) and phosphate-buffered saline (PBS, 10 × concentrate), 3-aminopropyltriethoxysilane (APTES, 99%), tetraethyl orthosilicate (TEOS, reagent grade), formaldehyde (for molecular biology, 36.5–38% in H_2O), hexadecyltrimethylammonium bromide (CTAB, >99%), sodium hydroxide (NaOH, BioXtra, ≥98%) were purchased from Sigma Aldrich. Zinc phthalocyanine tetrasulfonate ($ZnPcS_4$) was supplied from Santa Cruz Biotechnology, Inc. (Santa Cruz®: sc-264509A). Human malignant melanoma cell line A375 was purchased from the European Collection of Authenticated Cell Cultures (ECACC no: 88,113,005). All chemicals and reagents utilized in the study were of analytical grade. Millipore water was used to prepare aqueous solutions throughout the study. All glassware was washed thoroughly with aqua regia solution.

2.2. Fabrication of $ZnPcS_4$/Ag-PeG-Fa nanohybrids

2.2.1. Synthesis of Citrate-Ag NPs

1 mL of $AgNO_3$ was mixed with 79 mL Millipore water in a three-neck flask under a reflux system followed by the addition of a 20 mL citrate solution containing 0.5 mL of tannic acid, 1% tri-sodium citrate, and Millipore water. The mixture was stirred at ~60 °C for a few minutes to obtain a yellow color solution of citrate-capped Ag NPs.

2.2.2. PEGylation of Ag NPs

To covalently graft SH-PEG_{2k}-NH_2 onto the surface of Ag NPs, 20 mg/mL of the PEG in PBS was added to 1 mL of citrate-coated Ag NPs to induce a ligand exchange reaction. The solution was stirred at room temperature for a few minutes and incubated for 2 h. Subsequently, the solution was centrifuged to remove the excess SH-PEG_{2k}-NH_2 and dispersed in PBS.

2.2.3. Attachment of $ZnPcS_4$ to the PEGylated-Ag NPs

1 mL of the PEGylated Ag NPs was mixed with 1 mL of ZnPcS4 PS and agitated gently overnight in the dark at room temperature. Centrifugation was performed at 14,000 rpm for 15 min followed by dispersing of the resultant nanohybrids in PBS.

2.2.4. Conjugation of FA to the $ZnPcS_4$/Ag-PEG nanohybrids

Before conjugation of FA to the nanohybrids, the carboxyl groups of FA were activated through EDC/NHS reactions. Briefly, 20 mg FA in DMSO was activated with 100 mg EDC and 100 mg NHS for 24 h. Dicyclohexylurea as a by-product was removed by centrifugation. Ice-cold acetone was added to the mixture to purify the mixture. The pellet was washed three times with ice-cold acetone and dried under the fume hood. The activated FA was then dissolved in a mixture of DMSO: PBS and mixed with 1 mL $ZnPcS_4$/Ag-PEG nanohybrids with continuous stirring for 1 h in light-protected conditions. The resulting $ZnPcS_4$/Ag-PEG-FA nanohybrids were then purified with centrifugation to remove the excess FA and dispersed in PBS.

2.3. Fabrication of $ZnPcS_4$/Ag@$mSiO_2$-Fa nanohybrids

2.3.1. Synthesis of $Ag@mSiO_2$ NPs

Core/shell silver-mesoporous silica NPs were fabricated via a facile one-pot process with some minor modifications [14, 15]. Silver nitrate and formaldehyde were used as a precursor and a reducing agent respectively while CTAB acted as a template and a stabilizer. TEOS provided a silica source for the shell passivation and the presence of NaOH supplied a basic catalyst medium. Briefly, a solution containing 20 mg CTAB, 240 μL NaOH (0.5 M), and 9.8 mL Millipore water was prepared and stirred at 80 °C for 10 min. 60 μL formaldehyde was then added dropwise to the solution followed by the addition of 240 μL, 0.1 M silver nitrate. In the next step, 80 μL TEOS was added while stirring at 80 °C for 2 h. The resultant NPs were then washed and centrifuged at 15, 000 rpm with anhydrous ethanol three times. The CTAB surfactant was removed by dispersing the NPs in NH_4NO_3 (6 mg/mL) ethanol solution and reacted at 60 °C for 30 min under vigorous stirring. Core/shell $Ag@mSiO_2$ NPs were washed and centrifuged several times with Millipore water.

2.3.2. Amination of the $Ag@mSiO_2$ NPs

To functionalize $Ag@mSiO_2$ with amino groups, the precipitate was dissolved in ethanol and 20 μL APTES was added and stirred at 60 °C for 2 h. The resultant NPs were washed and centrifuged with ethanol several times followed by dispersing in Millipore water.

2.3.3. Loading of $ZnPcS_4$ PS into $Ag@mSiO_2$-NH_2 NPs

The loading of $ZnPcS_4$ PS into $Ag@mSiO_2$—NH_2 NPs was carried out by dispersing 1 mL of the PS in 1 mL of the NPs and agitating overnight in the dark. The excess $ZnPcS_4$ was removed by washing the loaded NPs with a mixture of ethanol/water (1:1) and centrifugation at 15,000 rpm. The prepared $ZnPcS_4$/$Ag@mSiO_2$—NH_2 nanohybrids were dispersed in PBS.

2.3.4. Attachment of FA to $ZnPcS_4$/Ag@$mSiO_2$-NH_2 nanohybrids

Carboxyl groups of FA were activated as explained in Section 2.2.4. 1 mL $ZnPcS_4$/$Ag@mSiO_2$—NH_2 nanohybrids was mixed with activated FA for 1 h to form amide bonds between carboxyl groups of FA and amino groups of the nanohybrids. The excess FA was separated by centrifugation at 15,000 rpm for some minutes and the prepared nanohybrids were dissolved in PBS to investigate their PDT effect on A375 cancer cells. The final targeted nanohybrids were referred to as $ZnPcS_4$/$Ag@mSiO_2$-FA throughout the paper.

2.4. Determination of the PS loading efficiency in the nanohybrids

To evaluate the amount of $ZnPcS_4$ loaded into the $Ag@mSiO_2$—NH_2 NPs (loading efficiency), the difference in the amount of initially added $ZnPcS_4$ to the NPs and the residual PS in the supernatant after centrifugation of the nanohybrids was measured via UV/Vis absorption spectroscopy. Therefore, 1 mL of $Ag@mSiO_2$—NH_2 NPs were mixed with 100 μL $ZnPcS_4$ (50 μM) overnight. The resultant solution was centrifuged and the absorbance difference between initial concentration and

supernatant was compared with a calibration curve of absorbance at 674 nm vs different concentrations of $ZnPcS_4$.

2.5. Physicochemical characterizations of the functionalized nanohybrids

A Jenway GenovaNano Plus Life Science Spectrophotometer was used to record the UV/Vis spectra of the NPs and nanohybrids. Fourier transform infrared (FT-IR) analysis was carried out using the Spectrum 100, FT-IR Spectrometer in the range of 400 - 4000 cm^{-1} with 25 scans. Malvern Zetasizer Nano ZS with a 4 mW He-Ne laser of 633 nm wavelength was utilized to explore the charge of the nanohybrids. The morphology and size of the NPs were estimated by using a transmission electron microscopy (TEM) instrument (JEOL, Gatan; Inc. Coronado Lane, Japan). Any changes in the cellular morphology of the A375 cells were evaluated 24 h after irradiation by using a light inverted microscope at 100 × magnification with a digital camera. A live imaging microscope (Carl Zeiss Axio Observer Z1) was used to check the localization of the nanohybrids.

2.6. In vitro experiments

2.6.1. Cell cultures

A375 melanoma cells were cultured in Dulbecco's Modified Eagle's medium (DMEM) medium supplemented with 10% (v/v) Fetal Bovine Serum (FBS), 0.1% (v/v) penicillin-streptomycin and 0.1% (v/v) amphotericin-β. The cells were incubated at 37 °C, with 5% CO_2.

2.6.2. Cellular uptake of the nanohybrids in A375 cells

1.0×10^5 cells/mL A375 cells were cultured on sterile coverslips in 3.4 cm diameter culture plates and incubated at 37 °C for cellular attachment. After 24 h incubation time, the media was replaced with fresh complete media containing the nanohybrids followed by 4 h incubation. The cells were then fixed on the coverslip with 4% paraformaldehyde followed by permeabilization with a solution containing 0.5% Triton X-100 in 1X PBS. The cells were then counterstained with 100 nM FITC-Mitotracker and 4′, 6-diamidino-2-phenylindole (DAPI) in the dark.

2.6.3. Dark toxicity assay of the znpcs4/ag-peg-fa nanohybrids

To assess the dark toxicity of the $ZnPcS_4$/Ag-PEG and $ZnPcS_4$/Ag@$mSiO_2$ nanohybrids (as control or passive targeted nanohybrids) and $ZnPcS_4$/Ag-PEG-FA and $ZnPcS_4$/Ag@$mSiO_2$-FA actively targeted nanohybrids, 2.5×10^5 cells/mL A375 cells were seeded and incubated for 24 h for cellular attachment. The cells were then treated with different concentrations of actively targeted nanohybrids ranging from 0.25 μM to 10 μM in fresh DMEM media followed by re-incubation in fresh media for an additional 4 h in the dark. The dark toxicity of 2.5 μM (IC_{50}) of $ZnPcS_4$/Ag-PEG and $ZnPcS_4$/Ag@$mSiO_2$ nanohybrids was also examined as a passive targeting control. The cells in culture media or a mixture of media and NPs alone were used as control groups. The cells were then lysed with Tryple™ Select and cell viability was measured with an ATP kit according to the manufacturer's protocol.

2.6.4. PDT assay of nanohybrids

The phototoxic effect of the passive and the final actively targeted nanohybrids were investigated with media containing different concentrations of $ZnPcS_4$/Ag-PEG-FA and $ZnPcS_4$/Ag@$mSiO_2$-FA nanohybrids and IC_{50} concentration of $ZnPcS_4$/Ag-PEG and $ZnPcS_4$/Ag@$mSiO_2$ nanohybrids (2.5 μM). The cells were cultured as described in Section 2.6.3. Following 4 h incubation of the cells with the nanohybrids, the cells were rinsed with HBSS. The PDT effect was performed in HBSS using light irradiation at 10 J/cm^2 doses with a semiconductor diode laser with an output power of 80 mW (light intensity: approximately 9 mW/cm^2) and the peak wavelength of 674 nm. All light irradiations were performed in the dark to prevent any additional light inferring reactions. After irradiation, fresh media was added followed by additional 24 h incubation until the ATP viability assay was performed. IC_{50} concentration by free $ZnPcS_4$ PS was found to be 2.5 μM in our group [16].

2.6.5. ATP viability assay

The cell viability of A375 cells was evaluated with various groups of nanohybrids, with and without light irradiation. Post 24 h incubation of the cells, as described in Section 2.6.4, the CellTiter-Glo® Luminescent cell viability assay (Promega, G7570) was utilized to measure the adenosine triphosphate (ATP) luminescence of the cells. Briefly, the cells were trypsinized with Tryple™ Select and washed with HBSS. An equivalent volume of cell suspension and ATP CellTiter-Glo® reagent was then mixed in a 96-well plate. VICTOR Nivo® multimode plate reader, (PerkinElmer, HH35940080 EN) was used to measure the luminescent signal of the cells and the signal was recorded in relative light units (RLUs). This experiment was carried out in triplicate, and the results are indicated as a percentage relative to the control.

2.7. Flow cytometry analysis

BD Accuri™ C6 flow cytometer through the Annexin V-FITC/PI cell death detection kit (BD Scientific: BD/556,570) was utilized to examine early or late apoptosis and necrosis pathways of the treated cells with the nanohybrids. A375 cells were cultured and incubated for 24 h for cellular attachment. The cells were then treated with passive and active targeted nanohybrids for 4 h. The treated cells were then divided into two subgroups with and without laser irradiation. After 24 h incubation, the cells were trypsinized and stained with Annexin V-FITC/PI.

2.8. ROS generation

ROS-Glo™ H_2O_2 Assay was performed to measure the generation of ROS in A375 cells treated with the passive and active targeted nanohybrids with/without 674 nm light irradiation. Briefly, 2×10^3 cells/well were seeded in 100 μL DMEM and incubated for 24 h for cellular attachment. The media was then replaced with fresh media containing both passive and active nanohybrids under the equivalent concentration of $ZnPcS_4$ followed by 4 h incubation and finally, the cells were irradiation at 674 nm. The treated cells were further incubated for 18 h and ROS assay was carried out based on manufacturer instruction where substrate solution was added in a final concentration of 25 μM and incubated for 6 h at 37 °C, 5% CO_2. ROS-Glo detection solution (100 μL) was then added to each well for 20 min. Relative luminescence units were recorded using VICTOR Nivo® multimode plate reader. This experiment was carried out in triplicate.

2.8. Statistical analysis

Biochemical assays were carried out three times. The student's *t*-test was utilized to compare two groups to assess the significant difference between the control and experimental groups in the 95% confidence interval. $P<0.05$*, $P<0.01$**or $P<0.001$*** were accepted as statistically different. Error bars referred to the standard deviation in the figures.

3. Results and discussion

3.1. Fabrication of the nanohybrids

Citrate-Ag NPs were synthesized in the presence of sodium citrate and tannic acid to reduce the metals. The coating of the NPs with citrate molecules provided enough stability to avoid aggregation of the NPs. PEGylation was then performed via Au-thiol bonds to replace the citrate capping with PEG molecules to enhance biocompatibility and avoid degradation or inactivation of the drug during transportation and decrease toxicity [17]. $ZnPcS_4$ PS was then adsorbed onto the surface of

the Ag-S-PEG-NH_2 through possible interactions of hydrogen bonding, van der Waals force, and electrostatic interactions [18]. Only hydrogen bonding between amino groups of the PEGylated NPs and oxygen (from sulfonate groups) of the PS is shown in Scheme 1A. Electrostatic interactions can also occur between the negatively charged $ZnPcS_4$ PS and positively charged amino groups of PEG molecules that did not react with FA. To provide active targeting moieties, the carboxylic groups of FA were activated through EDC/NHS reaction to form amide bonds with amino groups of the PEGylated NPs as indicated in Scheme 1A.

Core/shell Ag@mSiO_2 NPs were synthesized through the simple one-pot synchronous approach [15]. Silver nitrate was reduced by formaldehyde to form silver NPs which were stabilized with CTAB. Due to the negative charge of TEOS, mesoporous silica shells cannot coat directly onto the surface of electronegative Ag NPs. Therefore, CTAB was utilized as a surfactant to change the surface charge of Ag NPs to a positive charge [19]. Upon the introduction of TEOS, electrostatic interactions occurred between the hydrolyzed form of TEOS (silicate oligomers) and CTAB-coated Ag NPs leading to the growth of bigger Ag NPs. Simultaneously, an association of silica-surfactant micelles and CTAB-stabilized Ag NPs fabricated the ordered mesostructured with Ag NPs [15]. The CTAB templates were removed by ion exchange to provide mesoporous silica for the loading of $ZnPcS_4$. The amino groups of silica could form hydrogen bonding, van der Waals force, and electrostatic interactions with sulfonate groups of $ZnPcS_4$ to retain the PS inside the pores. Finally, attachment of activated FA to amino groups of the Ag@mSiO_2 NPs was performed as described above (Scheme 1B).

The loading amount of the PS in the $ZnPcS_4$/Ag-PEG-FA and $ZnPcS_4$/Ag@mSiO_2-FA based on the regression equation was estimated to be 22.0 and 22.3 μM respectively.

3.2. Characterizations of the nanohybrids

The formation of NPs and nanohybrids was monitored by using UV/Vis absorption spectroscopy. LSPR absorption peak of the citrate-Ag NPs was located at ~410 nm (Fig. 1A) while it showed a red-shift after PEGylation which can be due to a change in the refractive index of the dielectric environment around the plasmonic NPs [20,21]. $ZnPcS_4$ showed two electronic bands: the Soret or B band ($S_0 \rightarrow S_2$, $\pi \rightarrow \pi^*$) located in the near UV and the Q band ($S_0 \rightarrow S_1$, $\pi \rightarrow \pi^*$) placed on the red region of the spectrum with maxima at ca. 337, 635, and 674 nm [22]. Q bands are the most important band for practical applications. The band at 635 nm is related to the dimer while the band at 674 nm shows the monomer form of $ZnPcS_4$ and only the monomeric form can effectively produce ROS for PDT applications [23]. As evident from Fig. 1A, the peak at 674 nm confirmed the presence of the PS which was used for irradiation. Further, FA possessed three maximum absorption peaks at wavelengths of 256, 283, and 365 nm [24]. From the absorption maxima at 365 nm, the incorporation of FA was proved (Fig. 1A).

UV/Vis absorption spectra of Ag@mSiO_2—NH_2 NPs and final actively targeted $ZnPcS_4$/Ag@mSiO_2-FA nanohybrids are also shown in Fig. 1A. Ag@mSiO_2—NH_2 had a strong plasmon peak at ~412 nm while absorption peaks at 674 nm and 365 nm represented the successful loading of $ZnPcS_4$ into the NPs and the formation of amide bonds between amino groups of Ag@mSiO_2—NH_2 NPs and carboxyl groups of FA, respectively. Importantly, the great spectral overlap between the plasmon absorption peak of the NPs and the B band of $ZnPcS_4$ (~340 nm) could increase the resonance coupling of these two species resulting in enhanced ROS generation and PDT efficacy.

The size and morphology of citrate-Ag and Ag@mSiO_2—NH_2 NPs together with the final targeted $ZnPcS_4$/Ag-PEG-FA and $ZnPcS_4$/Ag@mSiO_2-FA nanohybrids were determined through TEM analysis. As illustrated in Fig. 1B (a) and (c), the sizes of the citrate-Ag and the core of Ag@mSiO_2—NH_2 NPs were found to be 28.2 ± 6.1 nm and 24.0 ± 6.2 respectively. As it can be seen from Fig. 1B (c), Ag NPs were embedded inside a fiber-like network which confirmed the presence of a silica shell on the surface of the silver core. After the attachment of the PS and FA to the Ag NPs (Fig. 1B (b)) and its loading into the Ag@mSiO_2—NH_2 NPs (Fig. 1B (d)), the morphology did not change and no agglomeration was

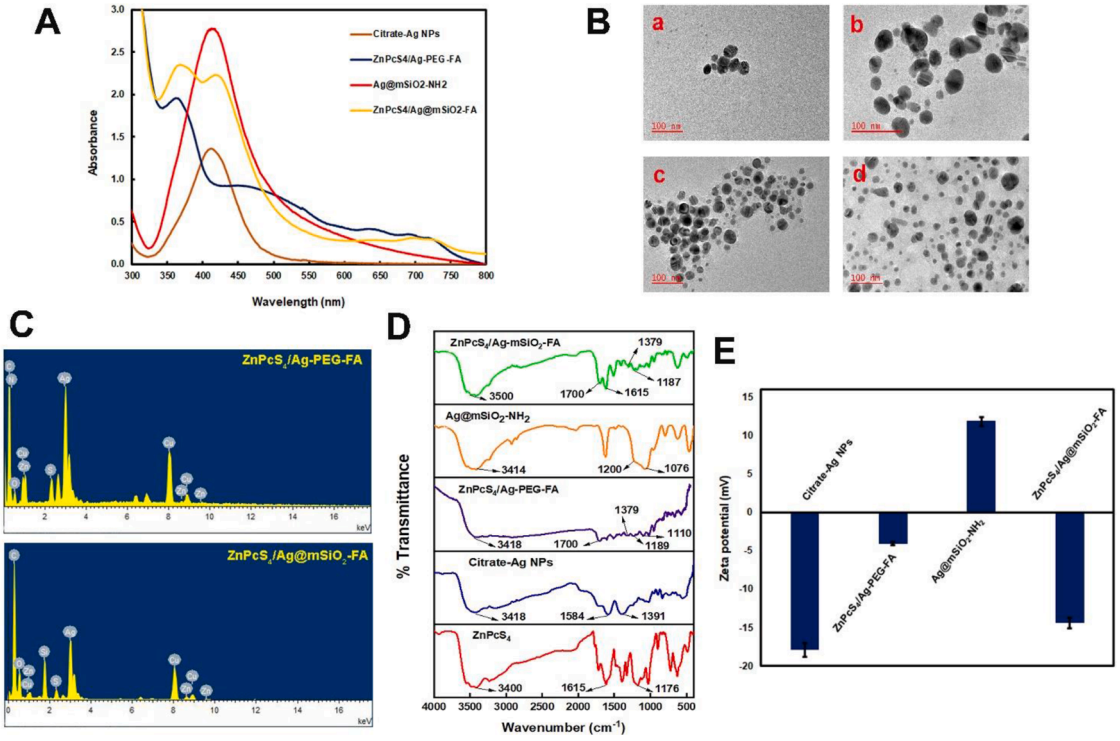

Fig. 1. Characterizations of the NPs and nanohybrids. (A) UV/Visible spectra of the NPs and final targeted nanohybrids, (B) TEM images (a) citrate-Ag NPs, (b) $ZnPcS_4$/Ag-PEG-FA, (c) core/shell Ag@mSiO_2—NH_2 NPs and (d) $ZnPcS_4$/Ag@mSiO_2-FA nanohybrids, (C) EDS spectra of $ZnPcS_4$/Ag-PEG-FA and $ZnPcS_4$/Ag@mSiO_2-FA nanohybrids, (D) FT-IR spectra of $ZnPcS_4$, citrate-Ag NPs, $ZnPcS_4$/Ag-PEG-FA nanohybrids, Ag@mSiO_2—NH_2 NPs, and $ZnPcS_4$/Ag@mSiO_2-FA nanohybrids, (E) Zeta potential of the synthesized NPs and actively targeted nanohybrids.

observed. Polydispersity index (PDI) of 0.35 ± 0.1 and 0.37 ± 0.04 for the $ZnPcS_4$/Ag-PEG-FA and $ZnPcS_4$/Ag@$mSiO_2$-FA respectively, indicated their excellent distribution with no aggregation [25].

Fig. 1C indicates EDS analysis of $ZnPcS_4$/Ag-PEG-FA and $ZnPcS_4$/Ag@$mSiO_2$-FA nanohybrids. It was found that $ZnPcS_4$/Ag-PEG-FA comprised of carbon (C), nitrogen (N), oxygen (O), sulfur (S), zinc (Zn), and silver (Ag) while silicon (Si) is an additional element in $ZnPcS_4$/Ag@$mSiO_2$-FA. Silver was the main element present in both nanohybrids and the copper (Cu) peaks associated with the grids used for EDS analysis.

Fourier transform infrared (FTIR) analysis was performed to indicate the presence of $ZnPcS_4$ and FA in the spectra of $ZnPcS_4$/Ag-PEG-FA and $ZnPcS_4$/Ag@$mSiO_2$-FA nanohybrids (Fig. 1D). Two absorption bands at 1584 and 1391 cm^{-1} in the spectra of citrate-Ag NPs were assigned to asymmetric and symmetric stretching vibrations of COO^- groups in the sodium citrate coating. The broad O—H peak at 3418 cm^{-1} was due to water molecules appearing in the NPs. The presence of SH-PEG-NH_2 was noted by the C—O-C stretching bands at 1110 cm^{-1} in the spectra of $ZnPcS_4$/Ag-PEG-FA. Moreover, the peak at 400–750 cm^{-1} pertained to the silver-thiol (Ag-S) bonds between Ag NPs and SH-PEG-NH_2 [26]. As for the spectra of Ag@$mSiO_2$—NH_2 NPs, the peak at 3414 cm^{-1} was attributed to N–H stretching from primary amine. Broadband at around 1076 cm^{-1} with a shoulder at around 1200 cm^{-1} was assigned to the asymmetric Si−O−Si linkage, which was evidence of the presence of silica in NPs. Additionally, absorption peaks in the range of 1195–1168 cm^{-1} and 1379–1335 cm^{-1} were related to S = O stretching from sulfonate groups of the $ZnPcS_4$ which confirmed the presence of the PS in both nanohybrids. After modification of the nanohybrids with FA, strong peaks appeared around 1700 cm^{-1} and 3500 cm^{-1} which showed the amide linkage for C = O stretching and N–H stretching respectively.

The electrokinetic potential known as zeta potential (ZP) is a powerful technique to assess the colloidal stability of NPs in solution. The ZP plots for the NPs and nanohybrids are shown in Fig. 1E and the corresponding values were −18.0 ± 2.9 mV for citrate-Ag NPs, −4.03 ±0.3 mV for $ZnPcS_4$/Ag-PEG-FA, 12.0 ± 0.8 mV for Ag@$mSiO_2$—NH_2 NPs and −14.4 ± 0.6 mV for the $ZnPcS_4$/Ag@$mSiO_2$-FA nanohybrids. Both synthesized NPs provided relative colloidal stability while the value obtained for $ZnPcS_4$/Ag@$mSiO_2$-FA showed higher stability compared to the $ZnPcS_4$/Ag-PEG-FA nanohybrids. Generally, a coating on NPs can enhance the stability of nanocarriers and facilitate drug loading. Additionally, small NPs tend to aggregate easily resulting in poor solubility of NPs in aqueous media or changing of the surface polarity/charge upon adsorption of molecules [17]. Therefore, surface coating, for example, silica can circumvent this issue to reduce the aggregation [27] and change the physicochemical properties of the surface, assisting further possibilities for drug adsorption [17].

From a cancer therapeutic point of view, metal NPs offer larger enhanced absorption cross-sections compared to photo-absorbing dyes resulting in efficient laser therapy at low energy [28]. They also have higher photostability with minimal photobleaching [28]. More importantly, encapsulation of the PSs into porous silica NPs can significantly improve photostability and singlet oxygen production [29,30] and protect the PS molecule from aggregation [29]. Figs. 2A and B illustrate the photostability of the final actively targeted $ZnPcS_4$/Ag-PEG-FA and $ZnPcS_4$/Ag@$mSiO_2$-FA nanohybrids in PBS over three months. The UV/Vis spectra of both nanohybrids showed no significant changes in Q bands of the PS (674 nm) or LSPR peak of the NPs suggesting that the nanohybrids remained stable with no aggregation. Broadening of the plasmon band in $ZnPcS_4$/Ag-PEG-FA arising from the negative charge of the nanohybrid surface due to the electron spill-out [31,32] and a slight decrease in the LSPR peak of $ZnPcS_4$/Ag@$mSiO_2$-FA can be attributed to a decrease in the electron density of the nanohybrid [31].

3.3. Cellular uptake examination of the nanohybrids

The intercellular localization of passive and actively targeted nanohybrids was evaluated under an equivalent concentration of the PS (2.5 μM) using live imaging microscopy. The distribution of the nanohybrids was monitored by red fluorescence of the PS in the presence of blue fluorescence of DAPI to stain nucleus and green FITC-stained Mitotracker and the results are shown in Fig. 3. Strong yellow fluorescence after 4 h incubation confirmed the successful cellular uptake of the PS in mitochondria. Although the cells treated with $ZnPcS_4$/Ag-PEG-FA and $ZnPcS_4$/Ag@$mSiO_2$-FA nanohybrids did not display a significant difference with the red fluorescence of passive nanohybrids, ATP, flow cytometry and ROS analysis confirmed higher PDT effect of the actively targeted nanohybrids. These results noted that the attachment of the nanohybrids with FA could increase photodynamic therapeutic effects for the active nanohybrids due to the overexpression of folate receptor (FR) in many types of cancers including A375 melanoma cells [33].

3.4. In vitro dark toxicity

The biocompatibility and PDT effect of the nanohybrids were evaluated using in vitro monolayer of A375 cells. In the dark toxicity assay, cell viability was assessed in the absence of light irradiation using the NPs and different concentrations of the nanohybrids over the range of 0.25–10 μM. The empty NPs (absence of $ZnPcS_4$ and FA) i.e., citrate-Ag NPs (Fig. 4A) and Ag@$mSiO_2$—NH_2 NPs (Fig. 4B) did not show any dark toxicity demonstrating good biocompatibility of the synthesized NPs. Additionally, the cells treated with neither passive targeted nanohybrids including $ZnPcS_4$/Ag-PEG (Fig. 4A) and $ZnPcS_4$/Ag@$mSiO_2$ (Fig. 4B) nor the final active targeted $ZnPcS_4$/Ag-PEG-FA nanohybrids (Fig. 4A) and $ZnPcS_4$/Ag@$mSiO_2$-FA (Fig. 4B) did not induce toxicity in the absence of light with the cell viability above 90%. Morphology images of the cells in the presence of both passive and actively targeted

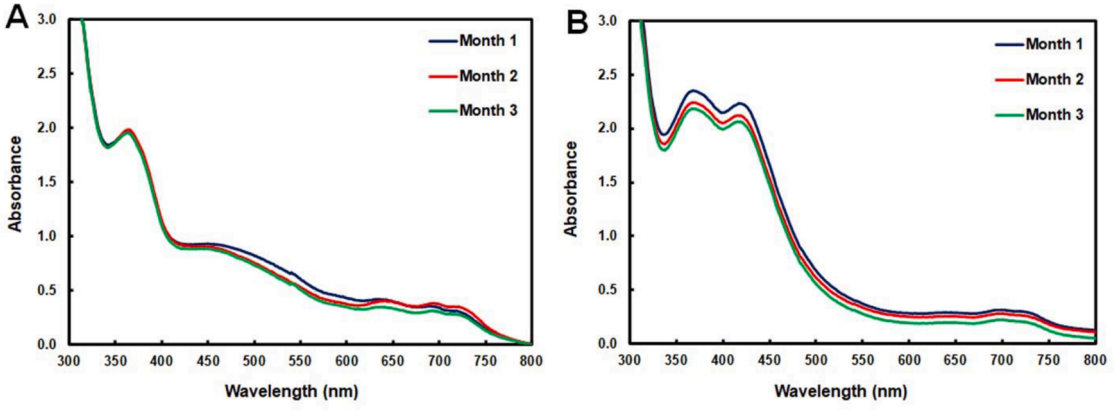

Fig. 2. Photostability of actively targeted (A) $ZnPcS_4$/Ag-PEG-FA and (B) $ZnPcS_4$/Ag@$mSiO_2$-FA nanohybrids in PBS over three months.

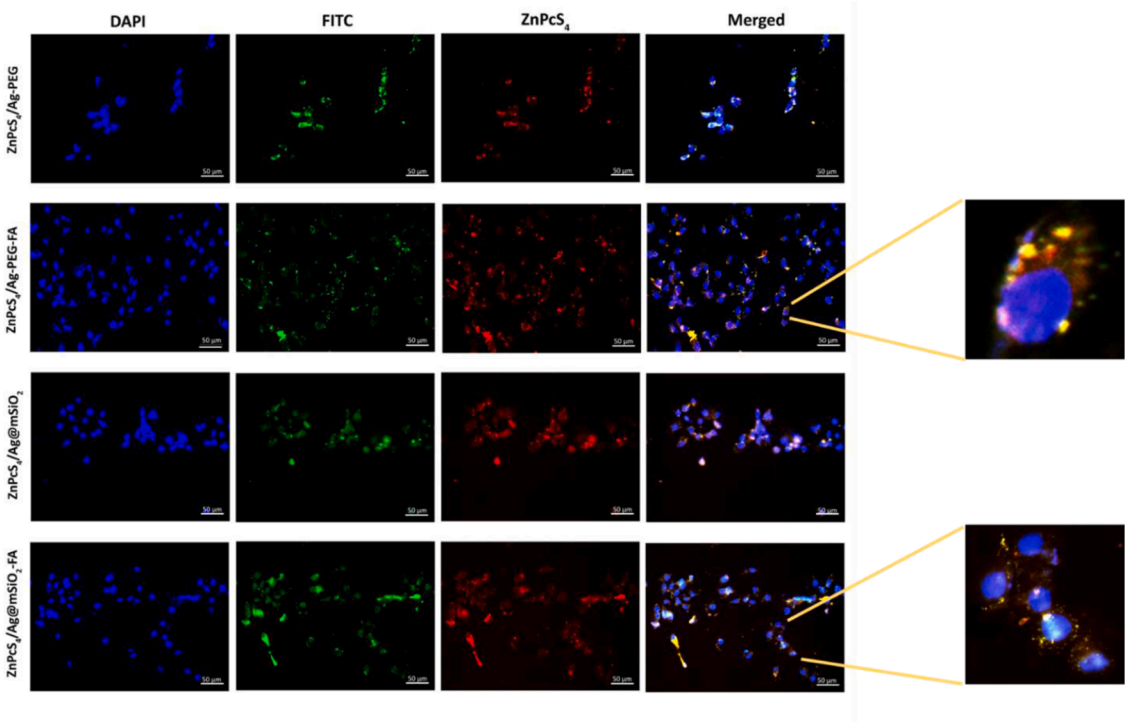

Fig. 3. Intercellular uptake of $ZnPcS_4$/Ag-PEG, $ZnPcS_4$/Ag-PEG-FA, $ZnPcS_4$/Ag@mSiO_2, and $ZnPcS_4$/Ag@mSiO_2-FA nanohybrids under the equivalent concentration of $ZnPcS_4$. The images in each row illustrate blue DAPI-stained nuclei, FITC-Mitotracker (green), $ZnPcS_4$ fluorescence (red), and their merged, respectively.

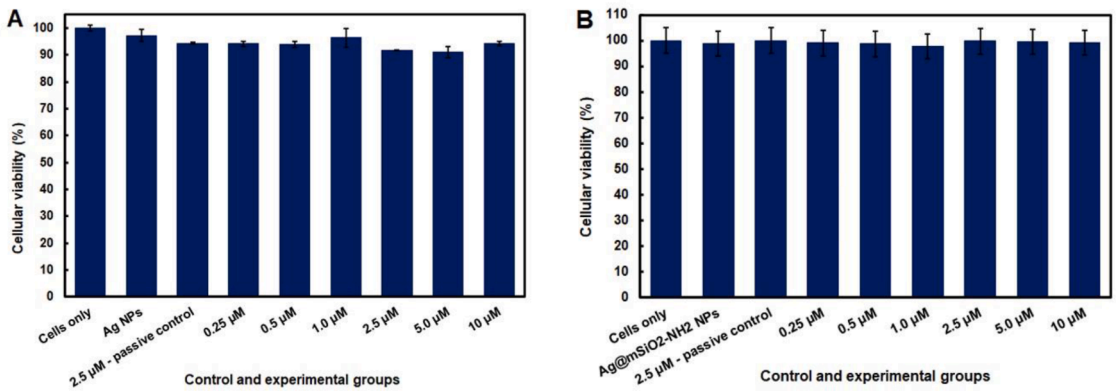

Fig. 4. Dark toxicity evaluation of control and experimental groups of (A) $ZnPcS_4$/Ag-PEG (passive control, under IC_{50}) and $ZnPcS_4$/Ag-PEG-FA nanohybrids and (B) $ZnPcS_4$/Ag@mSiO_2 (passive control, under IC_{50}) and $ZnPcS_4$/Ag@mSiO_2-FA nanohybrids.

nanohybrids with no irradiation also confirmed no significant changes or toxic effects and the distinctive appearance of the cells retained (Fig. 5).

3.5. PDT-Induced growth inhibition of tumor cells

Laser-initiated PDT applied on A374 cells at a wavelength of 674 nm using a fluence of 10 J/cm^2 noted the IC_{50} of 2.5 μM for the free $ZnPcS_4$ PS [34]. Under the same PDT conditions, empty NPs did not produce any significant viability changes. In sharp contrast, viability decreases from 43.1%* ± 2.0 for passive targeted to 30.4%* ±2.0 for actively targeted $ZnPcS_4$/Ag-PEG-FA nanohybrids (Fig. 6A) while $ZnPcS_4$/Ag@mSiO_2-FA nanohybrids noted 8.2%* ± 1.1 viability under half-maximal inhibitory concentration (IC_{50}, 2.5 μM) (Fig. 6B). The data in Fig. 5 confirmed that both actively targeted nanohybrids under 10 J/cm^2 fluence could induce significant harmful effects in dose-dependent inhibition viability. The IC_{50} value for the final actively targeted $ZnPcS_4$/Ag-PEG-FA and $ZnPcS_4$/Ag@mSiO_2-FA nanohybrids to A375 cells were found to be 0.5 μM and 0.25 μM respectively, which is much lower than that for the free $ZnPcS_4$ (2.5 μM). The superior performance of targeted FA nanohybrids was assigned to the enhanced cellular uptake. Furthermore, treatment with 2.5 μM of $ZnPcS_4$ incorporated in the Ag-PEG and Ag@mSiO_2—NH_2 NPs and FA induced ~70%* ± 2.9 and ~92%* ± 1.1 of cell death respectively against 50% (IC_{50}) for free $ZnPcS_4$.

Interestingly, $ZnPcS_4$/Ag@mSiO_2-FA nanohybrids noted lower IC_{50} and more cell death relative to the $ZnPcS_4$/Ag-PEG-FA nanohybrids. It was concluded that loading of the PS in the interior of the mesoporous silica shells can closely pack $ZnPcS_4$ with its silver core of Ag@m-SiO_2—NH_2 NPs resulting in enhancing efficient encapsulation [17] and preventing enzymatic degradation [29]. More importantly, due to plasmon resonance, energy transfer (PRET) between the $ZnPcS_4$ PS and the NPs, the energy harnessed from the light is transferred to the PS which is in extremely close vicinity of the silver core of Ag@mSiO_2—NH_2 NPs, thereby activating the PS indirectly. As a result, the excited PS

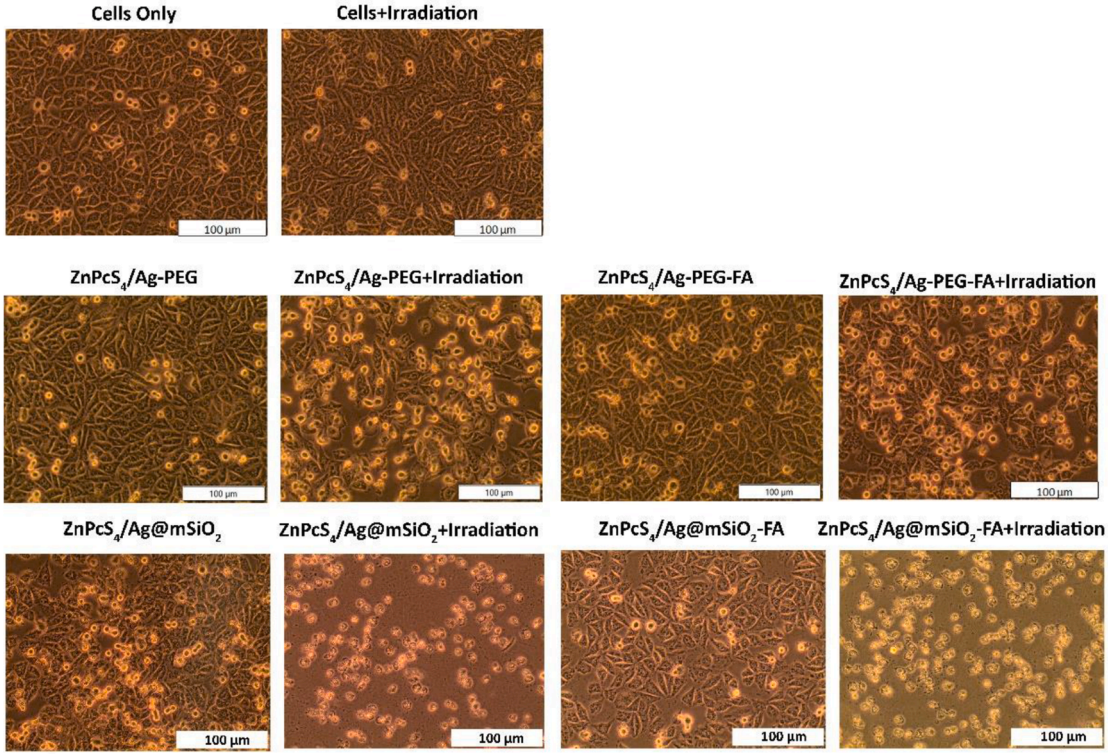

Fig. 5. Cell morphology images for PDT on A375 cells with the passive ($ZnPcS_4$/Ag-PEG and $ZnPcS_4$/Ag@$mSiO_2$) and actively targeted silver-based-nanohybrids ($ZnPcS_4$/Ag-PEG-FA and $ZnPcS_4$/Ag@$mSiO_2$-FA) and with/without laser irradiation under IC_{50} concentration of $ZnPcS_4$ (2.5 μM) at a wavelength of 674 nm and a fluence of 10 J/cm^2. A375 cells that received PDT (PS/Irradiation) showed significant morphological changes of rounding up in shape, nuclear destruction, and detached cells from the plates in comparison to the control groups which received only PS or irradiation.

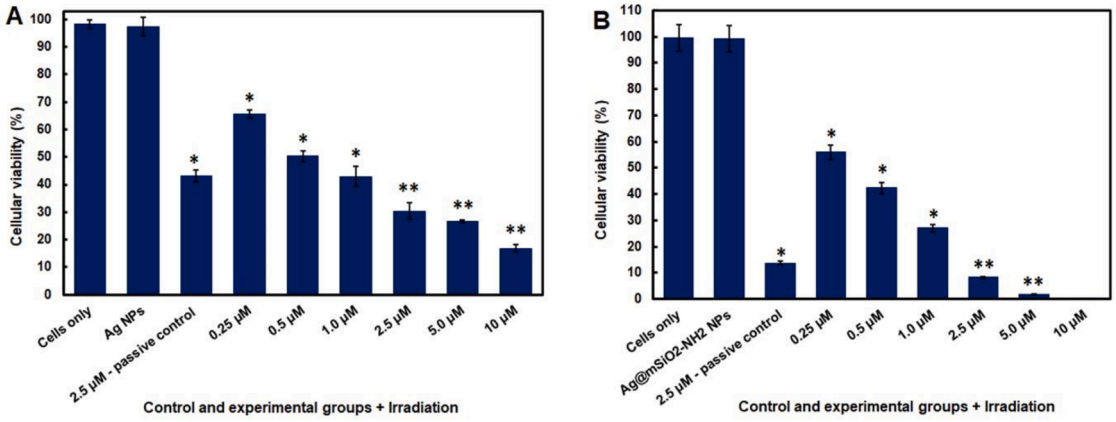

Fig. 6. ATP cell viability assay for (A) $ZnPcS_4$/Ag-PEG (passive control, IC_{50}) and $ZnPcS_4$/Ag-PEG-FA nanohybrids and (B) $ZnPcS_4$/Ag@$mSiO_2$ (passive control, IC_{50}) and $ZnPcS_4$/Ag@$mSiO_2$-FA nanohybrids ($P < 0.05$*, $P < 0.01$**). All experimental groups were compared with control group (cells only).

transfers its energy to molecular oxygen, thus generating further ROS compared to the PS only or $ZnPcS_4$/Ag-PEG-FA and providing higher PDT efficacy and more cell death which was proved with ROS generation analysis. However, in the case of $ZnPcS_4$/Ag-PEG-FA nanohybrids, the presence of large SH-PEG-NH_2 molecules on the surface of the Ag NPs may limit energy transfer between the PS and PEGylated NPs compared to the $ZnPcS_4$/Ag@$mSiO_2$-FA nanohybrids resulting in lower ROS generation and PDT effect (Section 3.7).

A research study demonstrated that strong resonance coupling between the PS and Ag core of the Ag@$mSiO_2$ NPs could form hybrid state (s) with new spectral characteristics. Additionally, the hybrids showed a significant increase in singlet oxygen generation by three orders of magnitude compared to the pure PS [35]. The hybrids also displayed satisfactory stability in singlet oxygen generation over a long illumination time, with no decrease in activity [35]. This type of PRET from plasmonic NPs to the PSs was further reported in other studies [36,37].

3.6. Flow cytometry analysis

Annexin V FITC/PI staining was carried out by using the flow cytometry 24 h after irradiation. Fig. 7 illustrates the data on A375 cell apoptosis and necrosis after different treatments with the nanohybrids. Generally, the PSs localized in mitochondria tend to induce apoptosis [38]. Therefore, photodamage to mitochondria leads to permeabilization of its membranes and leakage of cytochrome c into the cytosol [39]. Comparing the treated cells with passive and active targeted

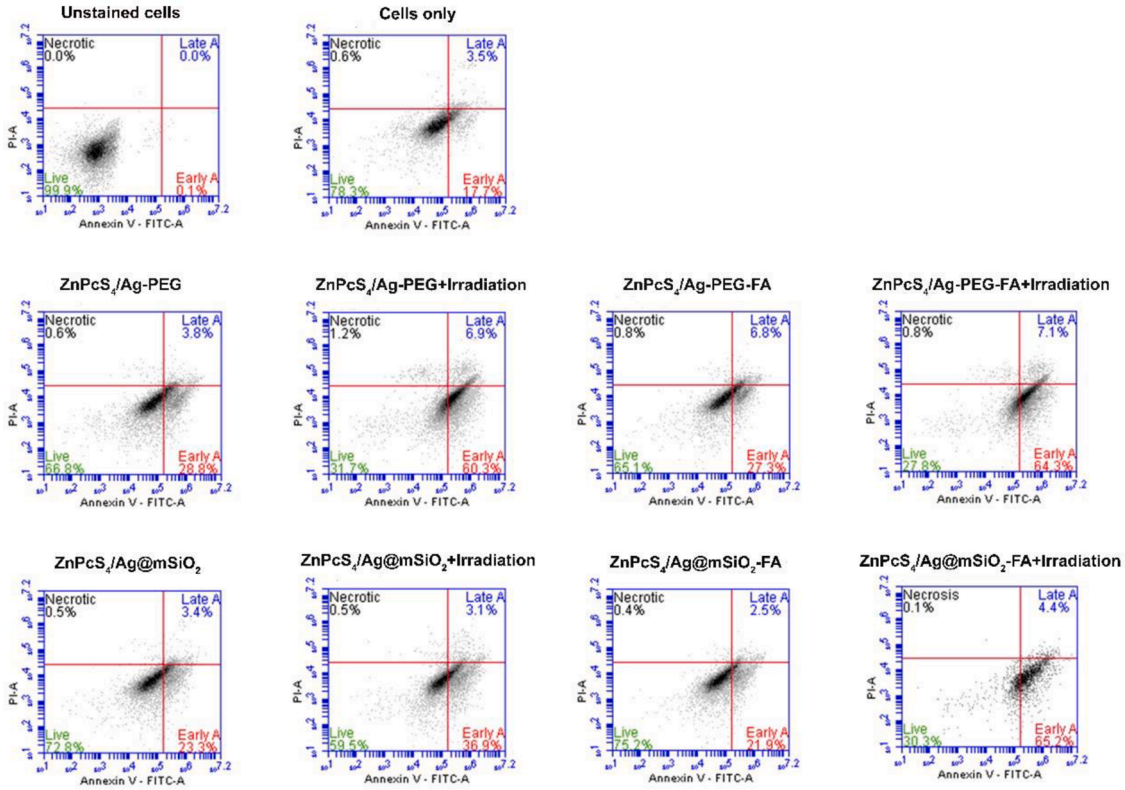

Fig. 7. Flow cytometry analysis using Annexin V-FITC/PI staining method on PDT treated A375 cells with passive and active targeted nanohybrids under the equivalent concentration of $ZnPcS_4$ (2.5 μM).

nanohybrids under 674 nm light irradiation, the percentage of apoptotic cells increased from 67.2%* ± 0.7 ($ZnPcS_4$/Ag-PEG) to ~71.4%** ± 5.3 ($ZnPcS_4$/Ag-PEG-FA) while it showed a rise from 40.0%* ± 4.6 for $ZnPcS_4$/Ag@$mSiO_2$ to 69.9.0%** ± 5.6 for $ZnPcS_4$/Ag@$mSiO_2$-FA. The results elicited that the targeting effect of folate-linked nanohybrids to tumor cells for $ZnPcS_4$/Ag@$mSiO_2$-FA was greater than $ZnPcS_4$/Ag--PEG-FA nanohybrids which arose most likely from the structure of SH-PEG-NH_2 molecules in latter nanohybrid and therefore it could not efficiently place in the vicinity of the folate receptors. However, $ZnPcS_4$/Ag-PEG and $ZnPcS_4$/Ag-PEG-FA nanohybrids showed a close percentage of apoptotic cells which was attributed to the relatively close amounts of ROS production (Section 3.7).

Although the apoptotic cells in $ZnPcS_4$/Ag-PEG-FA nanohybrids were nearly close to that of $ZnPcS_4$/Ag@$mSiO_2$-FA, the latter nanohybrids noted a remarkable increase between passive (40.0%* ± 4.6) and active (69.9.0%** ± 5.6) nanohybrids which supported the notable photodynamic therapeutic effect of the $ZnPcS_4$/Ag@$mSiO_2$-FA nanohybrids to obliterate melanoma cancer cells. It is important to emphasize that the conjugation of carboxyl groups of FA with the amino groups of the nanohybrids did not compromise the ability of FA to bind to folate receptors as the folate receptors reside on the surface of the cells [40,41]. Overall findings of this analysis were consistent with those of ATP assay and testified that $ZnPcS_4$/Ag@$mSiO_2$-FA nanohybrids plus irradiation could induce A375 cells to undergo apoptosis and can be a promising nanohybrid platform for PDT of melanoma cancer cells. It should also be borne in mind that apoptotic cells do not cause detrimental effects on their adjacent cells and they are the most favorable forms of cell death in PDT rather necrotic cell death pathway which releases harmful cellular waste [42].

It should be borne in mind that ATP assay is an indirect measurement to determine the number of viable cells based on quantitation of the ATP present, which is a marker for the presence of metabolically active cells. However, the ATP assay can only quantify whether the cells are dead and demonstrate the effect of PDT. Many factors can affect this assay such as cell confluency, metabolic rate, and cell activity. Hence, this assay may mistake these changes as cell death even though the cells are perfectly viable while flow cytometry is more reliable and precise to calculate the number of dead/live cells and distinguish various forms of cell death.

3.7. ROS generation analysis

To further explore the PDT effect of the nanohybrids, the level of intercellular ROS was evaluated for the cells treated with the passive and active nanohybrids with and without light irradiation. Singlet oxygen, hydroxyl radical, hydrogen peroxide, and superoxide are considered reactive oxygen species (ROS). Measurement of hydrogen peroxide in the cultured cell is convenient as it has the longest half-life. Additionally, various ROS are converted to H_2O_2 within cells [43,44]. Therefore H_2O_2 level can be used to evaluate the level of ROS produced in cells [44]. As can be seen in Fig. 8, $ZnPcS_4$/Ag@$mSiO_2$-FA+Irradiation produced elevated ROS intensity compared with $ZnPcS_4$/Ag@$mSiO_2$+Irradiation which was due to the presence of active targeting moieties and the results were in agreement with the flow cytometry. In addition, the cells exposed to $ZnPcS_4$/Ag-PEG and $ZnPcS_4$/Ag-PEG-FA under light irradiation did not show a significant difference in the level of ROS production which was concluded that the large structure of SH-PEG-NH_2 molecules (as explained in Section 3.5) may restrain the overexpression of nanohybrids on folate receptors.

4. Conclusions

Two highly effective nanohybrids based on the silver-core structure including Ag-PEG and Ag@$mSiO_2$ NPs were fabricated and attached to $ZnPcS_4$ PS. In these nanoplatforms, FA was integrated to enhance their overexpression on melanoma tumor cells. Both $ZnPcS_4$/Ag-PEG-FA and

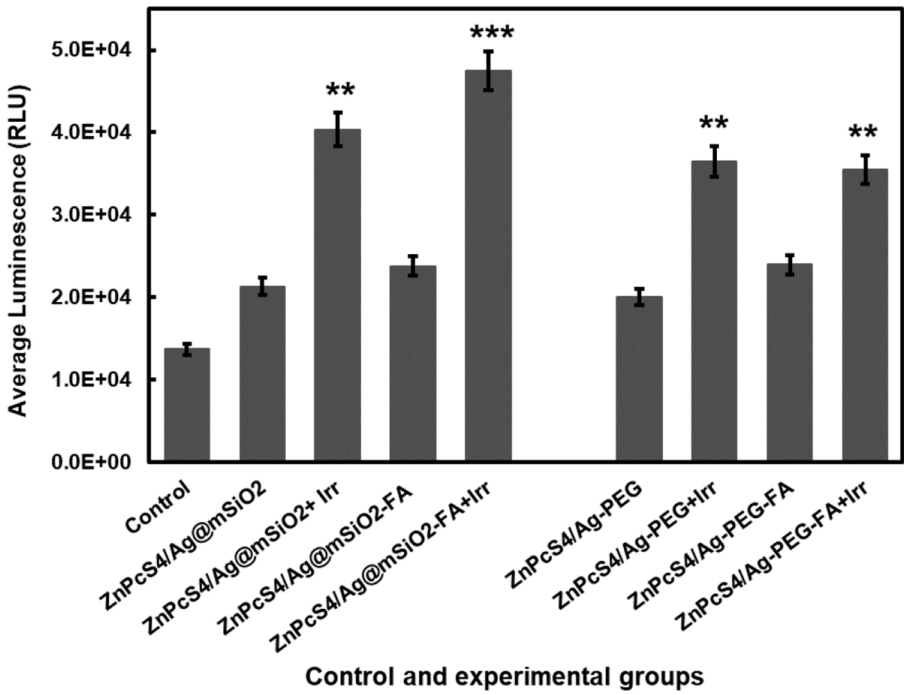

Fig. 8. Intercellular ROS generation in A375 cells subjected to treatment with passive and active nanohybrids under the equivalent concentration of ZnPcS4 and 674 nm light irradiation.

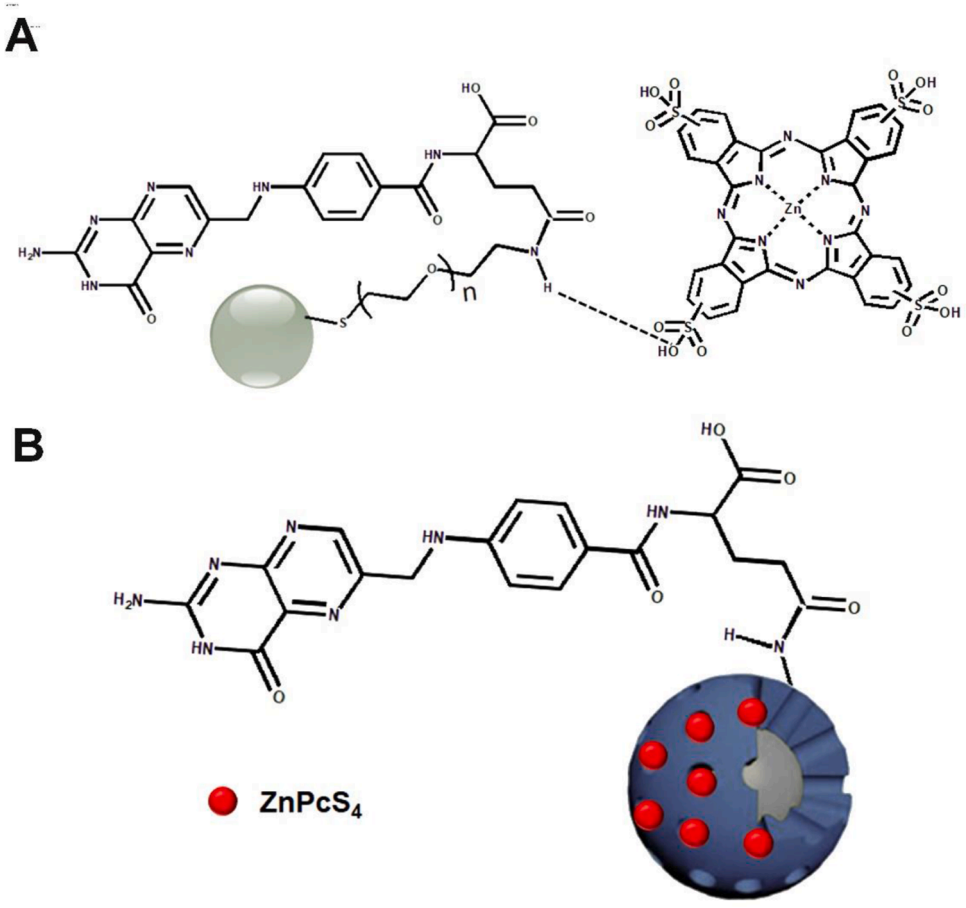

Scheme 1. Schematic illustration of (A) $ZnPcS_4$/Ag-PEG-FA (B) $ZnPcS_4$/Ag@$mSiO_2$-FA nanohybrids.

$ZnPcS_4$/Ag@mSiO_2-FA nanohybrids exhibited excellent dispersity while the latter nanohybrids provided higher colloidal stability in physiological solutions. The decoration of nanohybrids with targeting moiety could significantly enhance their cellular uptake confirming the successful uptake of $ZnPcS_4$-loaded nanohybrids into the mitochondria via folate receptors. The preliminary toxicity analysis showed that they have no obvious in vitro dark toxicity with high biocompatibility. While under 674 nm light irradiation, the $ZnPcS_4$/Ag@mSiO_2-FA nanohybrids could efficiently produce enough ROS for PDT with approximately 92%* ± 1.1 cell death relative to 70%* ± 2.9 for $ZnPcS_4$/Ag-PEG-FA due to high energy transfer between Ag@mSiO_2 NPs and PS. Summarizing our study proved that $ZnPcS_4$/Ag@mSiO_2-FA nanohybrids offer a simple yet effective treatment option against melanoma cancer cells which also reinforces the idea that the use of $ZnPcS_4$/Ag@mSiO_2-FA in vivo studies will achieve high PDT efficacy after optimization.

Declaration of Competing Interest

The authors declare no conflict of interest. This manuscript is based on our original research and has neither been published nor is being considered elsewhere for publication. Additionally, all the authors note that they do not have any relationships that they believe could be construed as a conflict of interest with regard to the manuscript review process.

Acknowledgments

The authors sincerely thank the University of Johannesburg, the National Laser center, and the National Research Foundation–South African Research Chairs Initiative (NRF-SARChI) for their financial grant support (grant number 98337). The authors sincerely thank the University of Johannesburg, the National Laser center, and the University of Johannesburg GES 4.0 PDF Fellow-ship for their financial grant support.

References

[1] B. Domingues, J.M. Lopes, P. Soares, H. Pópulo, Melanoma treatment in review, Immuno. Targets Ther. 7 (2018) 35.
[2] M.A. Wilson, L.M. Schuchter, Chemotherapy for melanoma, Melanoma (2016) 209–229.
[3] M.S. Soengas, S.W. Lowe, Apoptosis and melanoma chemoresistance, Oncogene 22 (2003) 3138–3151.
[4] E. Austin, A. Mamalis, D. Ho, J. Jagdeo, Laser and light-based therapy for cutaneous and soft-tissue metastases of malignant melanoma: a systematic review, Arch. Dermatol. Res. 309 (2017) 229–242.
[5] D. Van Straten, V. Mashayekhi, H.S. De Bruijn, S. Oliveira, D.J. Robinson, Oncologic photodynamic therapy: basic principles, current clinical status and future directions, Cancers 9 (2017) 19.
[6] Y. Huang, G. Xu, Y. Peng, H. Lin, X. Zheng, M. Xie, Zinc phthalocyanine tetrasulfonate (ZnPcS4): a new photosensitizer for photodynamic therapy in choroidal neovascularization, J. Ocul. Pharmacol. Ther. 23 (2007) 377–386.
[7] D.N. Zacks, E. Ezra, Y. Terada, N. Michaud, E. Connolly, E.S. Gragoudas, J. W. Miller, Verteporfin photodynamic therapy in the rat model of choroidal neovascularization: angiographic and histologic characterization, Invest. Ophthalmol. Vis. Sci. 43 (2002) 2384–2391.
[8] S. Wei, J. Zhou, D. Huang, X. Wang, B. Zhang, J. Shen, Synthesis and Type I/Type II photosensitizing properties of a novel amphiphilic zinc phthalocyanine, Dyes Pigm. 71 (2006) 61–67.
[9] F. Hu, Y. Huang, G. Zhang, R. Zhao, H. Yang, D. Zhang, Targeted bioimaging and photodynamic therapy of cancer cells with an activatable red fluorescent bioprobe, Anal. Chem. 86 (2014) 7987–7995.
[10] P.G. Mahajan, N.C. Dige, B.D. Vanjare, S.-.H. Eo, S.-.Y. Seo, S.J. Kim, S.-.K. Hong, C.-.S. Choi, K.H. Lee, A potential mediator for photodynamic therapy based on silver nanoparticles functionalized with porphyrin, J. Photochem. Photobiol. A. Chem. 377 (2019) 26–35.
[11] J. Rak, P. Pouckova, J. Benes, D. Vetvicka, Drug delivery systems for phthalocyanines for photodynamic therapy, Anticancer Res. 39 (2019) 3323–3339.
[12] J. Zeng, W. Yang, D. Shi, X. Li, H. Zhang, M. Chen, Porphyrin derivative conjugated with gold nanoparticles for dual-modality photodynamic and photothermal therapies in vitro, ACS Biomater. Sci. Eng. 4 (2018) 963–972.
[13] Y. Sun, F. Ding, Z. Zhou, C. Li, M. Pu, Y. Xu, Y. Zhan, X. Lu, H. Li, G. Yang, Rhomboidal Pt (II) metallacycle-based NIR-II theranostic nanoprobe for tumor diagnosis and image-guided therapy, Proc. Natl. Acad. Sci. 116 (2019) 1968–1973.
[14] N. Wijesiri, Z. Yu, H. Tang, P. Zhang, Antifungal photodynamic inactivation against dermatophyte Trichophyton rubrum using nanoparticle-based hybrid photosensitizers, Photodiagn. Photodyn. Ther. 23 (2018) 202–208.
[15] L. Han, H. Wei, B. Tu, D. Zhao, A facile one-pot synthesis of uniform core-shell silver nanoparticle@mesoporous silica nanospheres, Chem. Commun. 47 (2011) 8536–8538.
[16] C. Naidoo, C.A. Kruger, H. Abrahamse, Targeted photodynamic therapy treatment of in vitro A375 metastatic melanoma cells, Oncotarget 10 (2019) 6079.
[17] N. Wang, X. Cheng, N. Li, H. Wang, H. Chen, Nanocarriers and their loading strategies, Adv. Healthc. Mater. 8 (2019), 1801002.
[18] K. Siriwardana, M. Gadogbe, S.M. Ansar, E.S. Vasquez, W.E. Collier, S. Zou, K. B. Walters, D. Zhang, Ligand adsorption and exchange on pegylated gold nanoparticles, J. Phys. Chem. C 118 (2014) 11111–11119.
[19] M. Tang, L. Wang, D. Zhao, D. Huang, Ag@ mSiO2@ Ag core–satellite nanostructures enhance the antibacterial and anti-inflammatory activities of naringin, AIP Adv. 11 (2021), 055217.
[20] G.-.Y. Yao, Q.-.L. Liu, Z.-.Y. Zhao, Studied localized surface plasmon resonance effects of Au nanoparticles on TiO2 by FDTD simulations, Catalysts 8 (2018) 236.
[21] N. Koizumi, T. Hanai, Dielectric properties of polyethylene glycols: dielectric relaxation in solid state (special issue on polymer chemistry, I), Bull. Inst. Chem. Res. Kyoto Univ. 42 (1964) 115–127.
[22] J. Mack, M.J. Stillman, Transition assignments in the ultraviolet− visible absorption and magnetic circular dichroism spectra of phthalocyanines, Inorg. Chem. 40 (2001) 812–814.
[23] B. Brozek-Pluska, A. Jarota, R. Kania, H. Abramczyk, Zinc phthalocyanine photochemistry by raman imaging, fluorescence spectroscopy and femtosecond spectroscopy in normal and cancerous human colon tissues and single cells, Molecules 25 (2020) 2688.
[24] Y. Zhang, J. Li, M. Lang, X. Tang, L. Li, X. Shen, Folate-functionalized nanoparticles for controlled 5-fluorouracil delivery, J. Colloid Interface Sci. 354 (2011) 202–209.
[25] X. Zhao, C.-.X. Yang, L.-.G. Chen, X.-.P. Yan, Dual-stimuli responsive and reversibly activatable theranostic nanoprobe for precision tumor-targeting and fluorescence-guided photothermal therapy, Nat. Commun. 8 (2017) 1–9.
[26] R.V. Lupusoru, D.A. Pricop, C.M. Uritu, A. Arvinte, A. Coroaba, I. Esanu, M. F. Zaltariov, M. Silion, C. Stefanescu, M. Pinteala, Effect of TAT-DOX-PEG irradiated gold nanoparticles conjugates on human osteosarcoma cells, Sci. Rep. 10 (2020) 1–14.
[27] M. Yang, T. Chen, W.S. Lau, Y. Wang, Q. Tang, Y. Yang, H. Chen, Development of polymer-encapsulated metal nanoparticles as surface-enhanced Raman scattering probes, Small 5 (2009) 198–202.
[28] X. Huang, P.K. Jain, I.H. El-Sayed, M.A. El-Sayed, Plasmonic photothermal therapy (PPTT) using gold nanoparticles, Laser. Med. Sci. 23 (2008) 217.
[29] J. Krajczewski, K. Rucińska, H.E. Townley, A. Kudelski, Role of various nanoparticles in photodynamic therapy and detection methods of singlet oxygen, Photodiagn. Photodyn. Ther. 26 (2019) 162–178.
[30] B. Zhao, J.-.J. Yin, P.J. Bilski, C.F. Chignell, J.E. Roberts, Y.-.Y. He, Enhanced photodynamic efficacy towards melanoma cells by encapsulation of Pc4 in silica nanoparticles, Toxicol. Appl. Pharmacol. 241 (2009) 163–172.
[31] B.S. Hoener, H. Zhang, T.S. Heiderscheit, S.R. Kirchner, A.S. De Silva Indrasekara, R. Baiyasi, Y. Cai, P. Nordlander, S. Link, C.F. Landes, Spectral response of plasmonic gold nanoparticles to capacitive charging: morphology effects, J. Phys. Chem. Lett. 8 (2017) 2681–2688.
[32] M.Zapata Herrera, J. Aizpurua, A.K. Kazansky, A.G. Borisov, Plasmon response and electron dynamics in charged metallic nanoparticles, Langmuir 32 (2016) 2829–2840.
[33] F.S. Majidi, E. Mohammadi, B. Mehravi, S. Nouri, K. Ashtari, A. Neshasteh-Riz, Investigating the effect of near infrared photo thermal therapy folic acid conjugated gold nano shell on melanoma cancer cell line A375, Artif. Cells Nanomed. Biotechnol. 47 (2019) 2161–2170.
[34] C. Naidoo, C.A. Kruger, H. Abrahamse, Targeted photodynamic therapy treatment of in vitro A375 metastatic melanoma cells, Oncotarget 10 (2019) 6079–6095.
[35] B. Hu, X. Cao, K. Nahan, J. Caruso, H. Tang, P. Zhang, Surface plasmon-photosensitizer resonance coupling: an enhanced singlet oxygen production platform for broad-spectrum photodynamic inactivation of bacteria, J. Mater. Chem. B. 2 (2014) 7073–7081.
[36] H. Zhang, H. Li, H. Fan, J. Yan, D. Meng, S. Hou, Y. Ji, X. Wu, Formation of plasmon quenching dips greatly enhances 1 O 2 generation in a chlorin e6–gold nanorod coupled system, Nano Res. 11 (2018) 1456–1469.
[37] C. Liu, H. Dong, N. Wu, Y. Cao, X. Zhang, Plasmonic resonance energy transfer enhanced photodynamic therapy with Au@ SiO2@ Cu2O/perfluorohexane nanocomposites, ACS Appl. Mater. Interfaces 10 (2018) 6991–7002.
[38] D. Kessel, J.J. Reiners Jr, Apoptosis and autophagy after mitochondrial or endoplasmic reticulum photodamage, Photochem. Photobiol. 83 (2007) 1024–1028.
[39] S. Wu, D. Xing, Mechanism of mitochondrial membrane permeabilization during apoptosis under photofrin-mediated photodynamic therapy, J. X-Ray Sci. Technol. 20 (2012) 363–372.
[40] M.M. El-Hammadi, A.V. Delgado, C. Melguizo, J.C. Prados, J.L. Arias, Folic acid-decorated and PEGylated PLGA nanoparticles for improving the antitumour activity of 5-fluorouracil, Int. J. Pharm. 516 (2017) 61–70.
[41] P.S. Low, S.A. Kularatne, Folate-targeted therapeutic and imaging agents for cancer, Curr. Opin. Chem. Biol. 13 (2009) 256–262.

[42] J.R. Melamed, R.S. Edelstein, E.S. Day, Elucidating the fundamental mechanisms of cell death triggered by photothermal therapy, ACS Nano 9 (2015) 6–11.
[43] P. Newsholme, E. Rebelato, F. Abdulkader, M. Krause, A. Carpinelli, R. Curi, Reactive oxygen and nitrogen species generation, antioxidant defenses, and β-cell function: a critical role for amino acids, J. Endocrinol. 214 (2012) 11–20.
[44] A.A. Alfadda, R.M. Sallam, Reactive oxygen species in health and disease, J. Biomed. Biotechnol. 2012 (2012).